

Measurement of the cross section of top quark-antiquark pair production in association with a W boson in proton-proton collisions at $\sqrt{s} = 13$ TeV

The CMS Collaboration

Abstract

The production of a top quark-antiquark pair in association with a W boson ($t\bar{t}W$) is measured in proton-proton collisions at a center-of-mass energy of 13 TeV. The analyzed data was recorded by the CMS experiment at the CERN LHC and corresponds to an integrated luminosity of 138 fb^{-1} . Events with two or three leptons (electrons and muons) and additional jets are selected. In events with two leptons, a multiclass neural network is used to distinguish between the signal and background processes. Events with three leptons are categorized based on the number of jets and of jets originating from b quark hadronization, and the lepton charges. The inclusive $t\bar{t}W$ production cross section in the full phase space is measured to be 868 ± 40 (stat) ± 51 (syst) fb. The $t\bar{t}W^+$ and $t\bar{t}W^-$ cross sections are also measured as 553 ± 30 (stat) ± 30 (syst) and 343 ± 26 (stat) ± 25 (syst) fb, respectively, and the corresponding ratio of the two cross sections is found to be 1.61 ± 0.15 (stat) $^{+0.07}_{-0.05}$ (syst). The results are consistent with the standard model predictions within two standard deviations, and represent the most precise measurement of these cross sections to date.

Submitted to the Journal of High Energy Physics

1 Introduction

The production of a top quark-antiquark pair ($t\bar{t}$) in association with a vector boson (W and Z bosons and photons, referred to collectively as V) in proton-proton (pp) collisions provides an experimental probe that is sensitive to the electroweak (EW) couplings of the top quark. These $t\bar{t}V$ processes can receive sizable contributions from phenomena beyond the standard model (SM) of particle physics [1–3]. The production process of $t\bar{t}$ in association with a W boson ($t\bar{t}W$) is different from the $t\bar{t}V$ processes with neutral bosons ($t\bar{t}Z$ and $t\bar{t}\gamma$) since a W boson cannot be radiated from the final-state top quarks. The production proceeds at leading order (LO) in quantum chromodynamics (QCD) and EW couplings from quark-antiquark initial states. At next-to-LO (NLO), additional contributions arise from (anti)quark-gluon initial states. These dominant production modes are illustrated with representative Feynman diagrams in Fig. 1.

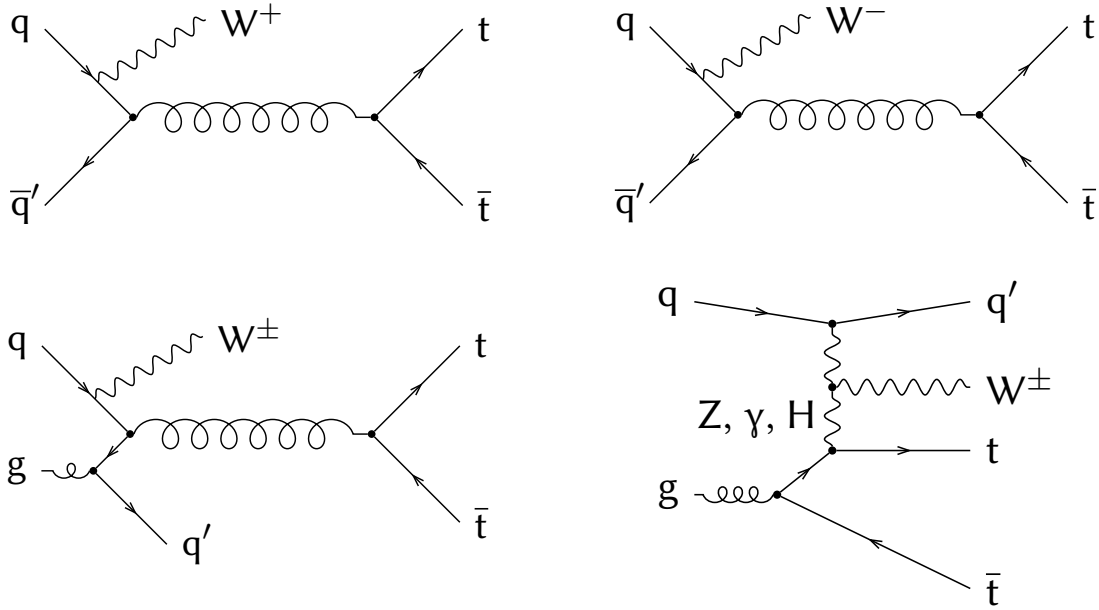


Figure 1: Representative Feynman diagrams of $t\bar{t}W$ production at LO (upper row) and NLO (lower row).

The absence of gluon-gluon initial states in $t\bar{t}W$ production leads to a sizable difference between production rates for the $t\bar{t}W^+$ and $t\bar{t}W^-$ processes because of differences in the parton distribution functions (PDFs) of the valence and sea quarks in the proton. Specifically, for the main LO production channels $u\bar{d} \rightarrow t\bar{t}W^+$ and $d\bar{u} \rightarrow t\bar{t}W^-$, the $u\bar{d}$ initial state has about twice the abundance of the $d\bar{u}$ initial state and typically a larger longitudinal quark momentum, resulting in a noticeable charge asymmetry [4]. Compared to the other $t\bar{t}V$ processes, the $t\bar{t}W$ process receives large corrections from the EW production diagrams at NLO, representing an important challenge in the calculation of the uncertainties for this process [5]. Therefore, precise cross section measurements are crucial inputs to further improve the calculations.

At the CERN LHC, $t\bar{t}W$ production has been measured at $\sqrt{s} = 7$ [6], 8 [7, 8], and 13 TeV [9–11]. In recent measurements of $t\bar{t}$ production in association with a Higgs boson ($t\bar{t}H$) [12] and the production of four top quarks ($t\bar{t}t\bar{t}$) [13, 14], a tension was observed between the observed and predicted yields for the $t\bar{t}W$ process, which represents one of the dominant backgrounds in these results. It has been shown that the observed difference can be attributed to missing NLO corrections in theoretical calculations for this process [15–22].

This paper presents a measurement of the inclusive $t\bar{t}W$ production cross section in the full phase space, based on an integrated luminosity of 138 fb^{-1} of pp collision data collected with

the CMS detector at $\sqrt{s} = 13$ TeV between 2016 and 2018. Two decay channels of the $t\bar{t}W$ system are analyzed, with either two same-sign or three charged leptons (any combination of electrons and muons, denoted as ℓ). The dominant background contributions arise from the presence of “nonprompt” leptons, which are leptons originating from hadron decays, as well as jets or hadrons that are misidentified as leptons. Suppression of these background events relies on multivariate analysis (MVA) techniques, which are optimized to distinguish between prompt leptons from the decay of W bosons and nonprompt leptons. Additional background contributions in final states with electrons arise from the misreconstruction of the electron charge and from the production of electrons in photon conversions. The dominant background contributions with prompt leptons are $t\bar{t}Z$ and $t\bar{t}H$ production, and the associated production of a W and Z boson (WZ). The $t\bar{t}W$ cross section is extracted from a profile likelihood fit to the data.

This analysis supersedes the CMS measurement presented in Ref. [10], which used data recorded in 2016, corresponding to an integrated luminosity of 35.9 fb^{-1} . In addition to the larger data set, the sensitivity is improved through the use of new machine-learning-based lepton and b hadron identification techniques. A more rigorous event categorization and improved background prediction techniques are also employed.

The paper is organized as follows: Section 2 gives a description of the CMS detector. In Section 3, the data set and simulated samples are described. In Section 4, the event reconstruction is defined. The event selection and analysis strategy are discussed in Section 5, followed by a description of the estimation of background processes in Section 6. The main sources of experimental and theoretical systematic uncertainties are presented in Section 7. Finally, the results and a summary are given in Sections 8 and 9, respectively. Tabulated results are provided in the HEPData record for this analysis [23].

2 The CMS detector

The central feature of the CMS apparatus is a superconducting solenoid of 6 m internal diameter, providing a magnetic field of 3.8 T. Within the solenoid volume are a silicon pixel and strip tracker, a lead tungstate crystal electromagnetic calorimeter (ECAL), and a brass and scintillator hadron calorimeter (HCAL), each composed of a barrel and two endcap sections. Forward calorimeters extend the pseudorapidity (η) coverage provided by the barrel and endcap detectors. Muons are detected in gas-ionization chambers embedded in the steel flux-return yoke outside the solenoid. A more detailed description of the CMS detector, together with a definition of the coordinate system used and the relevant kinematic variables, can be found in Ref. [24].

Events of interest are selected using a two-tiered trigger system. The first level (L1), composed of custom hardware processors, uses information from the calorimeters and muon detectors to select events at a rate of around 100 kHz within a fixed latency of about $4 \mu\text{s}$ [25]. The second level, known as the high-level trigger, consists of a farm of processors running a version of the full event reconstruction software optimized for fast processing, and reduces the event rate to around 1 kHz before data storage [26].

3 Data and simulated samples

The pp collision data used for this measurement have been recorded with a set of triggers that require the presence of one, two, or three reconstructed leptons. Simulated event samples are used to evaluate the signal selection efficiency, validate the background estimates with non-

prompt leptons, predict the background contributions with prompt leptons, and train MVA classifiers. Three separate sets of simulated event samples are used, corresponding to the conditions of the three data-taking years.

For the simulation of the $t\bar{t}W$ signal process at NLO accuracy, terms of the order $\alpha_S\alpha^3$ (EW term) and $\alpha_S^3\alpha$ (QCD term) are relevant [27], where α_S and α are the strong coupling and fine-structure constants, respectively. Events are simulated with the MADGRAPH5_aMC@NLO v2.6.0 [28] program, taking both the EW [2, 19] and QCD terms into account. The theoretical cross section used to normalize the combined simulated $t\bar{t}W$ event sample is 592_{-97}^{+155} (theo) fb, which is obtained at NLO in QCD and EW effects, and includes QCD corrections at next-to-next-to-leading-logarithmic (NNLL) accuracy [16]. The uncertainty in the prediction accounts for matrix-element scale variations and the PDF choice.

The MADGRAPH5_aMC@NLO program is also used to simulate background events at NLO accuracy for the production of $t\bar{t}$ or a single top quark in association with a vector boson ($t\bar{t}\gamma$, $t\bar{t}Z$, tZq , and $t\gamma$), as well as of $t\bar{t}\bar{t}$, Drell–Yan (DY), VVV, WZ, and VH production. Background processes for single top quark production in association with a Higgs boson (tHq and tHW) and for $t\bar{t}VV$ production are simulated with MADGRAPH5_aMC@NLO at LO accuracy. The POWHEG v2 [29–31] program is used to simulate events for the production of two W (WW) or two Z bosons (ZZ), $t\bar{t}$, and $t\bar{t}H$ at NLO precision. The background from SM events composed uniquely of jets produced through the strong interaction, referred to as QCD multijet events, is simulated at LO with PYTHIA v8.226 (v8.230) [32] in 2016 (2017–2018), and is used for the validation of background predictions associated with processes involving nonprompt leptons.

All samples are processed with the PYTHIA parton shower simulation. In the event simulation using MADGRAPH5_aMC@NLO, the FxFx [33] (MLM [34]) merging scheme is used for NLO (LO) samples, in order to avoid possible double counting between the matrix-element and parton shower calculations. The propagation of simulated particles through the CMS detector and modeling of the detector response is performed using the GEANT4 toolkit [35]. The simulated samples include inelastic pp interactions in the same or nearby bunch crossing (pileup), assuming a value of 69.2 mb for the total inelastic pp cross section [36, 37].

In the simulation used for the 2017–2018 data, the NNPDF3.1 [38] sets are used for the PDFs, and the underlying event is modeled with the CP5 tuning parameters [39, 40]. The 2016 samples for most processes are simulated using the same PDF sets and parton shower tune. For some background processes, however, the 2016 samples are modeled using the NNPDF3.0 [41] PDF sets, and with the CUETP8M1 [42] or CUETP8M2T4 [43] tunes.

4 Event reconstruction

The particle-flow (PF) algorithm [44] aims to reconstruct and identify each individual particle in an event, with an optimized combination of information from the various elements of the CMS detector. The energy of photons is obtained from the ECAL measurement. The energy of electrons is determined from a combination of the track momentum at the main interaction vertex, the corresponding ECAL cluster energy, and the energy sum of all bremsstrahlung photons attached to the track. The primary interaction vertex is taken to be the vertex corresponding to the hardest scattering in the event, evaluated using tracking information alone, as described in Section 9.4.1 of Ref. [45]. The energy of muons is obtained from the curvature of the corresponding track. The energy of charged hadrons is determined from a combination of their momentum measured in the tracker and the matching ECAL and HCAL energy deposits, corrected for the response function of the calorimeters to hadronic showers. Finally, the energy

of neutral hadrons is obtained from the corresponding corrected ECAL and HCAL energies.

Electrons are identified with an MVA discriminant [46] and are required to have transverse momentum $p_T > 10$ GeV and $|\eta| < 2.5$. Electrons that are reconstructed within the transition region between the barrel and the endcap sections of the detector within $1.479 < |\eta| < 1.566$, as well as those associated with tracks with more than one missing hit in the tracking system, are excluded from the analysis.

Muons are identified as tracks in the central tracker consistent with either a track or several hits in the muon system, and associated with calorimeter deposits compatible with the muon hypothesis. Reconstructed muons must have $p_T > 10$ GeV and $|\eta| < 2.4$, and fulfill selection criteria on the geometrical matching of the tracks reconstructed in the silicon tracker and the muon system, and on the quality of the global fit [47].

The “isolation” of a lepton is defined as the sum of the p_T of all reconstructed PF particles inside a cone of $\Delta R = \sqrt{(\Delta\eta)^2 + (\Delta\phi)^2} < R_{\max}$ (where $\Delta\eta$ and $\Delta\phi$ are the η and the azimuthal angle differences, respectively) around the direction of the lepton, excluding the lepton itself. We use a variable cone size that depends on the lepton p_T , defined as $R_{\max} = 10/\min[\max(p_T, 50), 200]$ (where p_T is given in GeV). The relative isolation, i.e., the isolation divided by the lepton p_T , is required to be less than 0.4. Any electron is furthermore required to be separated from any muon by $\Delta R > 0.05$.

The impact parameter of a lepton track with respect to the primary interaction vertex, with components in the transverse (d_{xy}) and longitudinal (d_z) planes relative to the direction of colliding proton beams, must satisfy $|d_{xy}| < 0.05$ cm and $|d_z| < 0.1$ cm, respectively. The impact parameter significance of the lepton track, defined as the absolute value of the ratio between the impact parameter value and its uncertainty, must be less than 8.

Two additional sets of lepton selection criteria, referred to as “loose” and “tight” in the following, are used to suppress background events associated with the presence of nonprompt leptons. The tight definition includes a requirement on a dedicated lepton MVA discriminant optimized for the selection of leptons in top quark events, which has been used in Refs. [48, 49] and is based on the earlier developments in Refs. [50, 51]. The prompt-lepton selection efficiency of this discriminant is evaluated in simulated event samples to be about 95% for leptons with $p_T > 25$ GeV, and 50–70% for leptons with $10 < p_T < 25$ GeV, depending on $|\eta|$. The loose definition includes all tight leptons and additionally leptons that fail the lepton MVA requirement but pass requirements on a number of input variables to the lepton MVA. Additionally, loose and tight electrons must not be associated with a secondary vertex that is consistent with a photon conversion [46], must have a charge measurement consistent among the three independent measurements described in Ref. [52], and fulfill additional criteria based on the shape of the electromagnetic shower and the consistency between the track and the shower [46].

In each event, jets are clustered from the reconstructed PF particles with the anti- k_T algorithm [53, 54] using a distance parameter of 0.4. The jet momentum is determined as the vector sum of the momenta of all particles in the jet, and is found from simulation to be, on average, within 5–10% of the true momentum over the entire p_T spectrum and detector acceptance. Additional tracks and calorimetric energy depositions can come from pileup, increasing the apparent jet momentum. To mitigate this effect, tracks identified as originating from pileup vertices are discarded and an offset correction is applied to correct for remaining contributions [55]. Jet energy corrections are derived from simulation studies so that the average measured energy of jets becomes identical to that of particle-level jets. In situ measurements of the momentum balance in dijet, photon+jet, Z+jet, and QCD multijet events are used to determine any residual

differences between the jet energy scale in data and simulation, and appropriate corrections are applied [56]. Additional selection criteria are applied to each jet to remove jets potentially dominated by instrumental effects or reconstruction failures [55]. Jets with $p_T > 25$ GeV and $|\eta| < 2.4$ are considered in the analysis, and those including a loose lepton among their PF constituents inside a cone of $\Delta R < 0.4$ are removed.

The DeepJet algorithm [57–59] is used to identify jets arising from the hadronization of b hadrons (b-tagged jets). The “loose” and “medium” b tagging selection requirements in this analysis correspond to selection efficiencies of about 90 and 85%, respectively, for b quark jets with $p_T > 30$ GeV as estimated in simulated $t\bar{t}$ events. For c quark jets (light quark and gluon jets), misidentification rates of 50 and 15% (10 and 1%) are obtained.

The missing transverse momentum vector \vec{p}_T^{miss} is computed as the negative vector sum of the \vec{p}_T of all reconstructed PF particles in an event, and its magnitude is denoted as p_T^{miss} [60]. The value of \vec{p}_T^{miss} is modified to account for corrections to the energy scale of the reconstructed jets in the event.

5 Event selection and analysis strategy

The measurement targets the $t\bar{t}W$ signal process in which the W boson decays to a lepton (electron or muon) and a neutrino, and the final state of the $t\bar{t}$ system includes either lepton+jets or dileptons. We select events containing two or three leptons. The dilepton and trilepton channels are analyzed separately, and combined for the final cross section measurement. To ensure that orthogonal event samples are used for the analyses of the two channels, only events with exactly two (three) loose leptons are considered in the dilepton (trilepton) channel. The signal regions of each channel are then defined by requiring that all of the loose leptons also pass the tight selection, which have further requirements discussed in the remainder of this section. Events with at least one loose-not-tight lepton are used in each channel for the estimation of the nonprompt-lepton backgrounds, as discussed in Section 6.

Same-sign dilepton channel: Events in the dilepton channel are required to have exactly two tight leptons and no additional loose leptons. We require that the two leptons have the same sign electric charge, which significantly reduces background contributions from SM processes with two opposite-sign prompt leptons (e.g., $t\bar{t}$ and DY production). The highest p_T (leading) lepton is required to have $p_T > 30$ GeV if it is an electron, or $p_T > 25$ GeV if it is a muon. The second-highest p_T (subleading) lepton is required to have $p_T > 20$ GeV, independent of flavor. To reduce background contributions from low-mass resonances and photon conversions, the dilepton invariant mass $m(\ell\ell)$ is required to be larger than 30 GeV, and the separation between the leptons must be $\Delta R > 0.4$. Events with two electrons and $|m(ee) - m_Z| < 15$ GeV are removed, where m_Z is the world-average Z boson mass [61]. The events are also required to have $p_T^{\text{miss}} > 30$ GeV and at least two jets, out of which at least two pass the loose b tagging selection or at least one passes the medium b tagging selection, which reduces background contributions from DY and ZZ production.

A multiclass neural network (NN) classifier is used to distinguish between events from the signal $t\bar{t}W$ process and those from three classes of background processes: $t\bar{t}Z$ and $t\bar{t}H$ as a combined category, $t\bar{t}\gamma$, and backgrounds with nonprompt leptons. The classifier is trained with the simulated $t\bar{t}W$, $t\bar{t}Z$, $t\bar{t}H$, and $t\bar{t}\gamma$ samples, and with simulated $t\bar{t}$ events as a source of nonprompt-lepton background events.

The NN has two fully connected hidden layers with 128 and 64 rectified linear units [62], re-

spectively, and an output layer with four nodes corresponding to the four categories defined above. The training is performed using the TENSORFLOW package [63] with the KERAS interface [64] and the ADAM optimizer [65]. The training phase aims at reducing the cross-entropy loss function [66], and potential overtraining is mitigated using dropout [67].

The value of each output node can be interpreted as the probability for a given event to belong to that corresponding category. We only use the $t\bar{t}W$ output node as a discriminant between signal and background events. The inclusion of the three separate background classes with significantly different kinematic properties in a multiclass NN leads to a better discriminating power compared to a binary classification approach, even if only a single output node is used. The final NN discriminant that is used in the fit is obtained from a monotonic transformation of the $t\bar{t}W$ output node value, which is designed to give an approximately linearly decreasing distribution of the total expected background.

The input variables include several kinematic observables associated with the reconstructed leptons and jets, such as p_T , ϕ , ΔR , and invariant masses calculated for several combinations of leptons and jets. Further input variables are the jet and b-tagged jet multiplicities, the b tagging discriminant values of the selected jets, information about the flavor and charge of the leptons, and p_T^{miss} . In Fig. 2, six of the input variables that provide the best discrimination between the four classes of events are shown. Overall, a reasonably good agreement between data and background predictions is observed, with some disagreement in the tails of the distributions. These discrepancies largely disappear once the results from the fit are incorporated. We have validated that the agreement between data and simulation for all the input variables is reasonable. Additional validations have been performed in the control regions defined in Section 6.

Trilepton channel: Events in the trilepton channel are required to have exactly three tight leptons, with $p_T > 25$ GeV for the leading lepton and $p_T > 15$ GeV for the other two leptons. It is required that $m(\ell\ell) > 12$ GeV for each pair of leptons to remove background contributions from low-mass resonances, and $|m(\ell\ell) - m_Z| > 10$ GeV for each pair of leptons of same flavor and opposite sign to remove DY contributions. The sum of charges of the three leptons is required to be ± 1 , and events must contain at least two jets, out of which at least one passes the medium b tagging selection.

The analysis strategy in the trilepton channel relies on an event categorization based on the number of jets and medium b-tagged jets, and on the charges of the selected leptons. The number of observed and predicted events in all twelve categories used in the fit is shown in Fig. 3. The invariant mass of the three leptons, $m(3\ell)$, was identified as the observable with the best discriminating power between signal and background contributions, and is used across all event categories as the discriminant variable.

6 Background estimation

The nonprompt-lepton background contributes to both the same-sign dilepton and trilepton channels. Its contribution is estimated from control samples in data using a tight-to-loose ratio method [12, 50, 68]. The lepton misidentification rate is defined as the probability f for a loose lepton to also satisfy the tight selection. It is parameterized as a function of the lepton p_T and $|\eta|$, and measured in a data sample enriched in QCD multijet events (“multijet sample”). The nonprompt-lepton background contribution in the signal channels is then estimated by applying the measured misidentification rate as a weight to events that pass the event selection but have at least one “loose-not-tight” lepton, i.e., a lepton that passes the loose but fails the

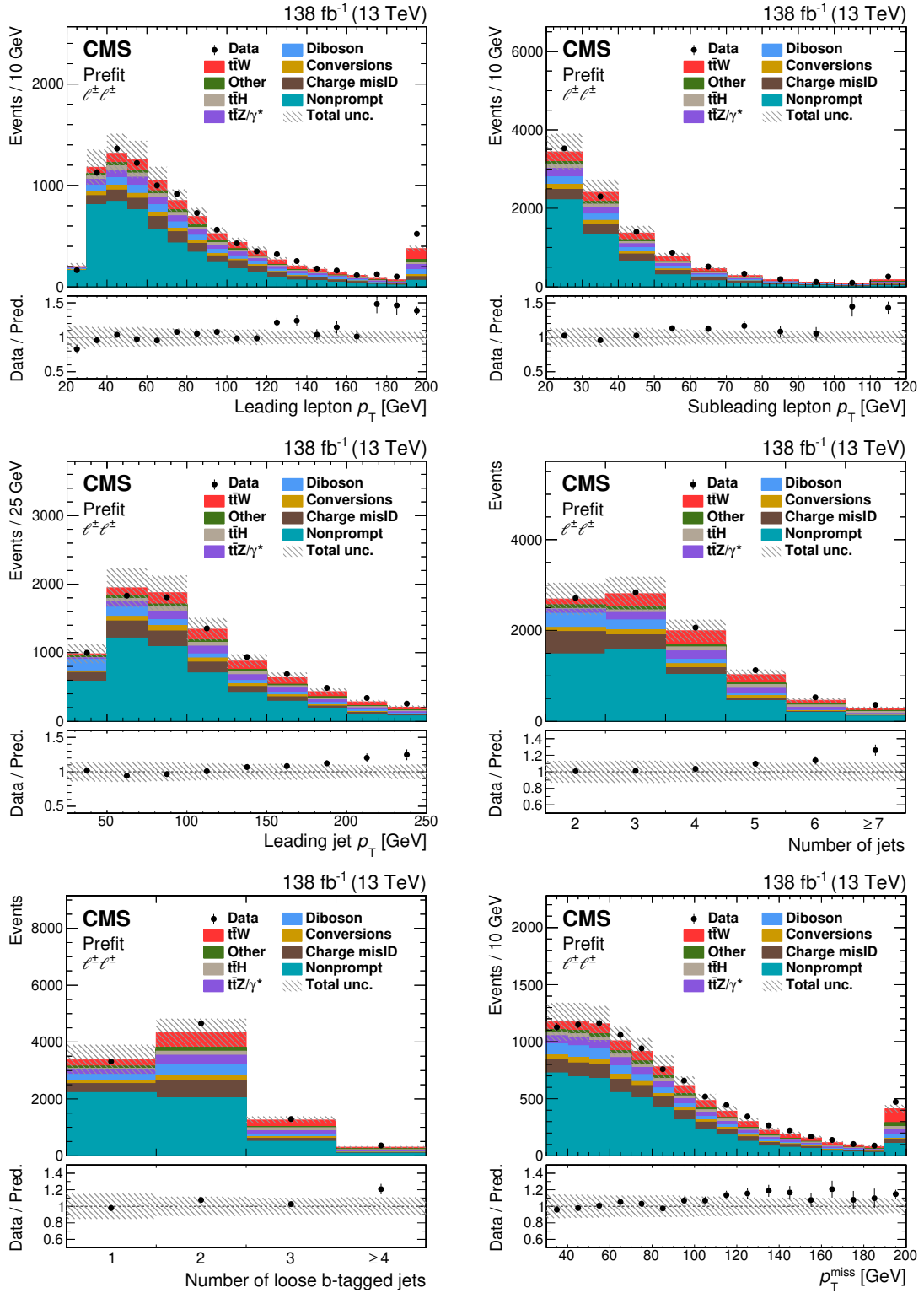


Figure 2: Comparison of the number of observed (points) and predicted (colored histograms) events in the same-sign dilepton signal region. The distributions of the leading (upper left) and subleading (upper right) lepton p_T , the leading jet p_T (middle left), the number of jets (middle right), the number of loose b-tagged jets (lower left), and p_T^{miss} (lower right) are displayed. The predictions are shown before the fit to data (“Predit”). The vertical bars on the points represent the statistical uncertainties in the data, and the hatched bands the systematic uncertainty in the predictions. The last bins include the overflow contributions. In the lower panels, the ratio of the event yields in data to the overall sum of the predictions is presented.

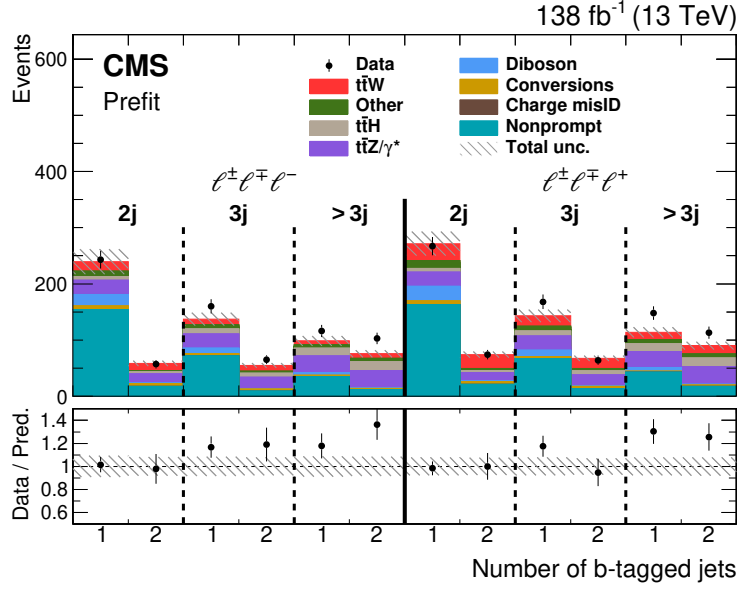


Figure 3: Distribution of the number of medium b-tagged jets per event from data (points) and prediction (colored histograms) for events in the trilepton signal region with different numbers of jets (j). Events with total trilepton charge -1 and $+1$ are shown in the left and right halves of the plot, respectively. The predictions are shown before the fit to data (“Prefit”). The vertical bars on the points represent the statistical uncertainties in the data, and the hatched bands the systematic uncertainty in the predictions. The lower panel shows the ratio of the event yields in data to the overall sum of the predictions.

tight selection (“loose-lepton sample”). The weights w are defined as

$$w = (-1)^{n+1} \prod_{i=1}^n \frac{f_i}{1 - f_i'} \quad (1)$$

where the product extends over all electrons and muons that pass the loose but fail the tight selection, and n refers to the total number of such leptons. In both the multijet and loose-lepton sample, the prompt-lepton contributions are estimated from simulated event samples and subtracted.

Events in the multijet sample are required to have exactly one loose lepton, at least one jet that is separated from the lepton by $\Delta R > 0.7$, and $p_T^{\text{miss}} < 20$ GeV to reduce contributions from prompt W +jets events. The numbers of multijet events with a loose-not-tight and a tight lepton are individually determined for each lepton p_T and $|\eta|$ bin from maximum likelihood fits to the transverse mass variable

$$m_T^{\text{fixed}} = \sqrt{2p_T^{\text{fixed}} p_T^{\text{miss}} [1 - \cos(\Delta\phi)]}, \quad (2)$$

where $p_T^{\text{fixed}} = 35$ GeV is a constant, and $\Delta\phi$ is the azimuthal angle between the lepton momentum and \vec{p}_T^{miss} . This m_T^{fixed} definition exploits the fact that the p_T^{miss} reconstructed in QCD multijet events is mainly due to resolution effects and is typically small, resulting in a falling distribution of m_T^{fixed} . In contrast, the m_T^{fixed} distribution for W +jets events, which is the main source of prompt-lepton backgrounds in the QCD multijet selection, has a broad maximum around 80 GeV. Since we use p_T^{fixed} instead of the reconstructed lepton p_T , the value of m_T^{fixed} does not depend on the latter [12]. In each p_T and $|\eta|$ bin, the lepton misidentification rate is then measured as $f_i = N_{\text{pass}} / (N_{\text{pass}} + N_{\text{fail}})$, where N_{pass} and N_{fail} are the numbers of events

where the lepton is loose-not-tight or tight, respectively, as extracted from the fit and after subtracting the fitted contributions from prompt leptons.

The nonprompt-lepton background prediction with the tight-to-loose ratio method is validated using same-sign dilepton events from data satisfying the full event selection but with a $p_T^{\text{miss}} < 30 \text{ GeV}$ requirement, making this validation region orthogonal to the signal region. The comparison of the distributions from data and prediction of four NN input variables in the validation region, shown in Fig. 4, shows good agreement. This is also true for the other NN input variables, demonstrating that the prediction provides a good description of the kinematic variables used in the NN training for the nonprompt-lepton background. This validation region is used to assign an additional systematic uncertainty in the nonprompt-lepton background prediction, as described in Section 7.

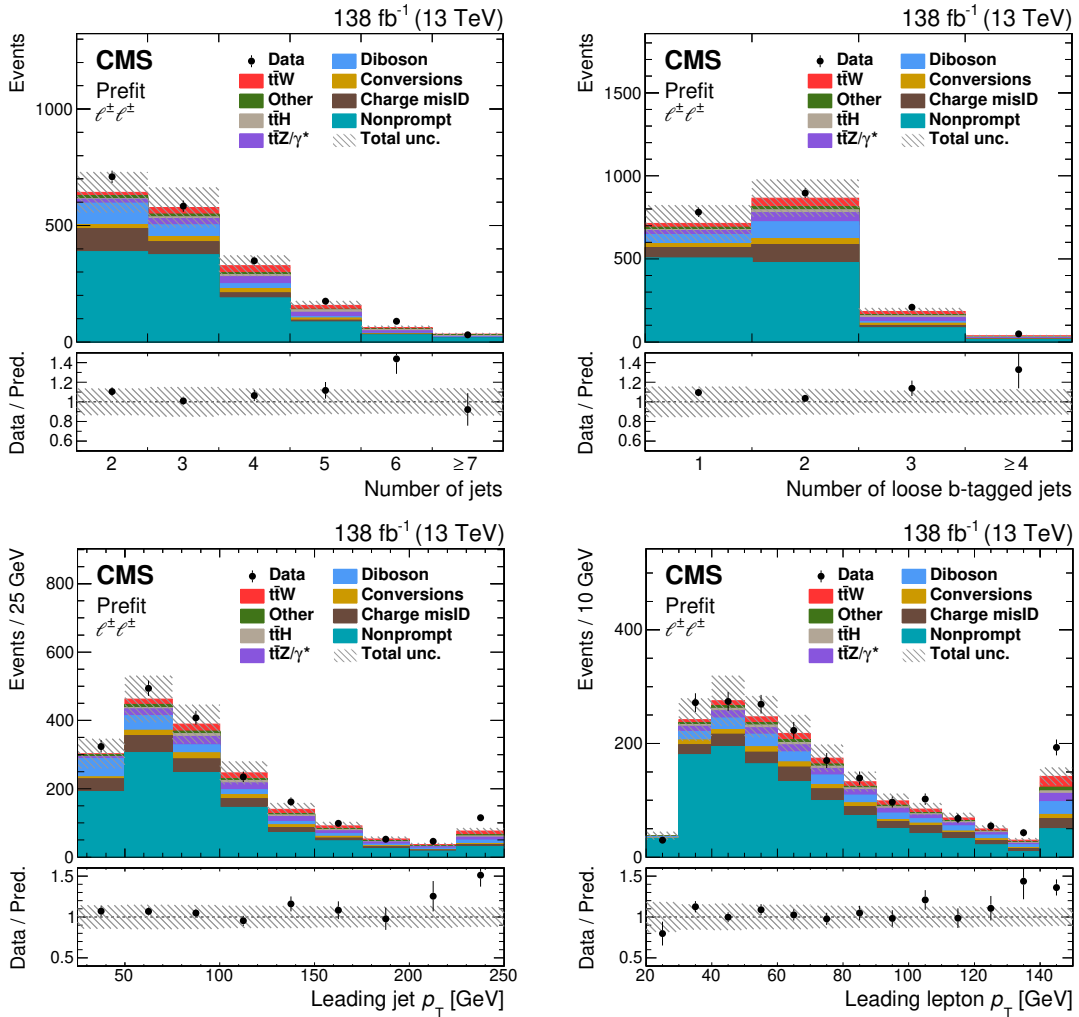


Figure 4: Comparison of the number of observed (points) and predicted (colored histograms) events in the validation region for nonprompt leptons. The distributions of the number of jets (upper left) and loose b-tagged jets (upper right), and of the p_T of the leading jet (lower left) and of the leading lepton (lower right) are displayed. The predictions are shown before the fit to data (“Predit”). The vertical bars on the points represent the statistical uncertainties in the data, and the hatched bands the systematic uncertainty in the predictions. The last bins include the overflow contributions. In the lower panels, the ratio of the event yields in data to the overall sum of the predictions is presented.

Background contributions arising from the mismeasured electron charge (indicated as “Charge misID” in the figures) are relevant in the same-sign dilepton channel. The mismeasurement of the electron charge is typically the result of the emission of a hard bremsstrahlung photon that undergoes asymmetric conversion. The reconstructed lepton is then typically the electron or positron that receives most of the energy of the converted photon, and thus has an equal probability to have either the same or opposite charge compared to the original electron or positron [46]. The charge misidentification rate is defined as the probability that the reconstructed charge of an electron differs from its true value. It is parameterized as a function of the lepton p_T and $|\eta|$, and is measured in simulated samples of DY and $t\bar{t}$ production using tight electrons. The predicted number of background events is estimated from data by applying the misidentification rates as weights to events that pass the dilepton event selection but have two opposite-sign electrons. The charge misidentification rate for muons was found to be negligible.

Background processes with one or more reconstructed electrons due to the conversion of a photon are estimated from simulated event samples. In these events, an electron or a positron typically carries most of the energy of the converted photon, while the other lepton is of low energy and not reconstructed. The largest source of events with electrons from photon conversions in the signal regions is from $t\bar{t}\gamma$ production.

Background contributions with prompt leptons are estimated from simulated event samples, and are normalized to the cross sections predicted from SM calculations. The main contributions arise from $t\bar{t}H$, $t\bar{t}Z/\gamma^*$, and diboson (WZ and ZZ) production. Smaller contributions, including VVV and rare top quark ($t\bar{t}VV$, $t\bar{t}t\bar{t}$, tHq , and tZq) production, are grouped together and are indicated as “Other” in the figures.

For the trilepton channel, the predictions from simulated event samples for the dominant processes with a Z boson (WZ, ZZ, and $t\bar{t}Z$) are validated using dedicated data control regions. Events are selected for a WZ and $t\bar{t}Z$ production control region by applying the full event selection except for the requirement on same-flavor opposite-sign lepton pairs, where we require that there be at least one pair with $|m(\ell\ell) - m_Z| < 10$ GeV. This ensures that the control region is orthogonal to the trilepton signal region. The events are grouped according to the number of jets and medium b-tagged jets, and the distributions of these quantities from data and prediction are compared in Fig. 5. The control region is further split into four categories based on the flavors of the selected leptons, which are included in the fit for the extraction of the $t\bar{t}W$ cross section.

A control region enriched in ZZ and $t\bar{t}Z$ events is defined by an event selection that requires exactly four tight leptons. Ordering the leptons in decreasing order of momentum, they are required to have $p_T > 25, 15, 15,$ and 10 GeV, respectively. Additionally, the presence of at least one Z boson candidate, defined as a same-flavor opposite-sign lepton pair with $|m(\ell\ell) - m_Z| < 10$ GeV, is required. The remaining events are then put into four groups: (1) events with two Z boson candidates; events with exactly one Z boson candidate and (2) zero jets, (3) ≥ 1 jet of which exactly one is a medium b-tagged jet, and (4) ≥ 2 jets of which more than one is a medium b-tagged jet. Events not passing any of these criteria are removed from the control region. The distributions of the number of jets and medium b-tagged jets for this control region are shown in Fig. 6 from data and prediction. The four groups are also included in the fit for the extraction of the $t\bar{t}W$ cross section, in order to constrain the normalization of the ZZ and $t\bar{t}Z$ backgrounds.

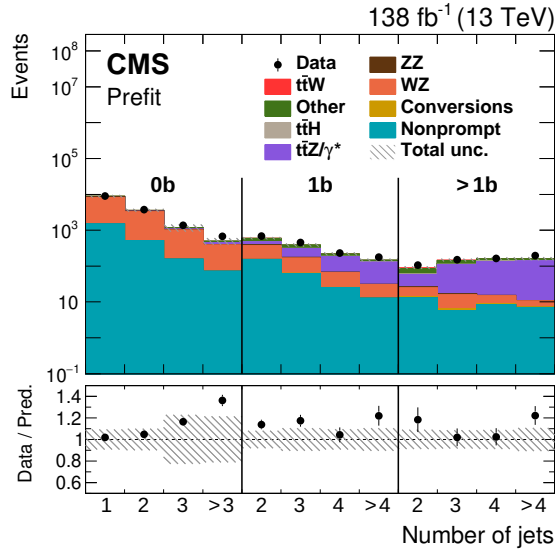


Figure 5: The distributions of the number of jets in events from the control region enriched in WZ and $t\bar{t}Z$ production from data (points) and prediction (colored histograms). The events are divided into three groups depending on the number of medium b-tagged jets b in the event. The predictions are shown before the fit to data (“Prefit”). The vertical bars on the points represent the statistical uncertainties in the data, and the hatched bands the systematic uncertainty in the predictions. In the lower panels, the ratio of the event yields in data to the overall sum of the predictions is presented.

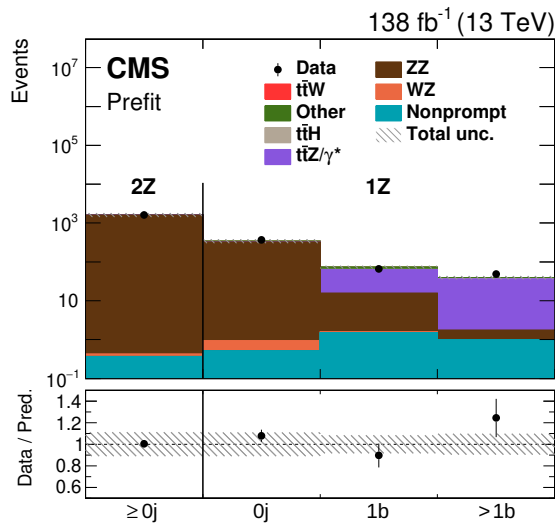


Figure 6: Distribution of the number of jets j and medium b-tagged jets b in events from the control region enriched in ZZ and $t\bar{t}Z$ events for data (points) and prediction (colored histograms). Events in the first bin have two Z boson candidates (2Z) and events in the other bins have exactly one Z boson candidate (1Z). The predictions are shown before the fit to data (“Prefit”). The small contribution from background processes with nonprompt leptons is estimated from simulated event samples. The vertical bars on the points represent the statistical uncertainties in the data, and the hatched bands the systematic uncertainty in the predictions. In the lower panels, the ratio of the event yields in data to the overall sum of the predictions is presented.

7 Systematic uncertainties

Multiple sources of systematic uncertainty affect the signal and background event yields and the distributions of the discriminating observables used for the signal extraction. These sources can be divided into two categories. Sources that affect only the yield of the signal or background processes are considered as rate uncertainties. Sources that modify the shape of the fitted distributions are referred to as shape uncertainties. The main sources of experimental and theoretical systematic uncertainties are described below.

Integrated luminosity: The integrated luminosities for the 2016, 2017, and 2018 data-taking years have individual uncertainties between 1.2 and 2.5% [69–71], while the overall uncertainty for the 2016–2018 period is 1.6%. The uncertainty in the integrated luminosity is a rate uncertainty and affects both the normalization of the background contributions from simulated event samples, as well as the extraction of the measured cross section from the final estimate of the number of signal events.

Pileup reweighting: The distribution of the number of additional pp interactions per event in simulation is matched to data by reweighting the profile of the true number of interactions to the one inferred from the instantaneous luminosity profile in data. A systematic uncertainty is estimated by varying the assumed minimum-bias cross section of 69.2 mb by $\pm 4.6\%$ [36, 37]. This variation is propagated throughout the analysis, yielding a shape uncertainty that is considered fully correlated among the data-taking years.

Trigger efficiency: The efficiency of the trigger selection is measured in data and simulated events using independent trigger paths based on hadronic activity or p_T^{miss} signatures. Per-event weights that depend on the lepton p_T are applied to the simulated samples in order to correct for discrepancies. The impact on the final discriminants due to the trigger efficiency uncertainty is estimated by varying these scale factors within their uncertainties, which are determined to be 2%. This shape uncertainty is treated as uncorrelated among data-taking years, as well as between the dilepton and trilepton channels. A separate uncertainty is determined for each lepton flavor category in the dilepton channel.

L1 inefficiency: During the 2016 and 2017 data-taking periods, a gradual shift in the timing of the inputs of the ECAL L1 trigger in the region at $|\eta| > 2$ caused a specific trigger inefficiency. For events containing an electron (a jet) with p_T larger than ≈ 50 GeV (≈ 100 GeV), in the region $2.5 < |\eta| < 3.0$ the efficiency loss is ≈ 10 –20%, depending on p_T , η , and time. Correction factors were computed from data and applied to the acceptance evaluated by simulation, resulting in a shape uncertainty that is correlated between 2016 and 2017. As expected in analyses that do not rely on forward objects, the effect on the results is small (below 1%).

Lepton efficiency: The efficiency of the tight-lepton selection is measured in data and simulation using the “tag-and-probe” method in $Z \rightarrow \ell^+ \ell^-$ events [46, 47]. Per-lepton corrections are derived separately for each lepton flavor, and a shape uncertainty is obtained and found to be at most a few percent in each bin. This is treated as correlated between data-taking years, and uncorrelated between the lepton flavors.

Jet energy scale and resolution: The variations of the jet momenta due to the uncertainty in the jet energy scale and resolution are composed of 21 uncertainty sources which account for different detector regions and the year-to-year correlations [56]. The uncertainties in the p_T^{miss} resolution and response are accounted for by varying the jet energy scale in simulation within their respective uncertainties and recomputing p_T^{miss} after each variation. The p_T^{miss} uncertainties are not relevant for the trilepton channel, where p_T^{miss} is not used. This resulting shape uncertainty is considered to be partially correlated between data-taking years.

b tagging efficiency: The uncertainty in the b tagging efficiency scale factors is considered to be fully correlated between b and c quark jets, and uncorrelated for other quark flavors. It is applied as a function of p_T and $|\eta|$ of the jets, and propagated as shape uncertainty to the fitted distributions. These sources are considered as partially correlated between data-taking years.

Background normalization: Several rate uncertainties are considered for the normalization of the background processes. The normalizations of the $t\bar{t}Z$, WZ, and ZZ background contributions are determined in the fit from the control regions described in Section 6. The WZ and ZZ events with a large number of b-tagged jets are either due to misidentified light-flavor jets, or to the inclusion of a phase space region that is not well described in simulation. This has been studied in Ref. [68], and we apply an additional 40 (10)% uncertainty to the predicted number of events with two or more (fewer than two) b-tagged jets, following those results. An additional uncertainty of 30% is applied to WZ and ZZ events with at least three selected jets in order to account for mismodeling effects observed in the corresponding control region described in Section 6. The normalization of the $t\bar{t}H$ background is constrained within a 20% uncertainty [12]. The normalization of the $t\bar{t}\gamma$ process includes an uncertainty of 8% [72]. To account for a possible mismodeling of photon conversions in the simulation, an additional 30% uncertainty is applied to the predicted number of events, following the studies performed in Ref. [73]. The normalizations of the tHq and tHW backgrounds are each constrained within a 50% uncertainty [74]. The tZq normalization uncertainty amounts to 10%, following the latest measurement done by CMS [48]. A 50% uncertainty is applied to the $t\bar{t}VV$ normalization, which reflects the current experimental precision [75]. A 50% uncertainty is estimated for the triboson production, as the main contribution to this background comes from the WWW production, studied in Ref. [76]. For other background processes with smaller production cross sections, the yields are constrained within 50%. Even if several of these processes have been measured to a higher precision, the assigned uncertainty conservatively takes into account the extrapolation of these predictions to the kinematic region important for this analysis, which contains events with high jet and b-tagged jet multiplicities.

Nonprompt-lepton background: The misidentification rates used to estimate the nonprompt-lepton background are affected by a statistical uncertainty associated with the multijet sample, as well as inaccuracies in the modeling of the contamination due to prompt leptons in this sample. For each lepton flavor, shape uncertainties are added to the prediction of the background processes with nonprompt leptons. These account for the overall normalization, as well as for the p_T and η dependence of the statistical uncertainty and the observed mismodeling effects. These are taken as correlated among the data-taking years. An additional systematic uncertainty of 20% is applied to the nonprompt-background estimate that covers the differences between the prediction and the observation in the validation region for nonprompt leptons. This systematic uncertainty is taken as correlated among the data-taking years and the considered final states.

Charge misidentification background: Due to the differences observed between the data and prediction in the validation region described in Section 6, we assign a rate uncertainty of 20% to the charge misidentification background. Since this background is negligible for the trilepton channel, this uncertainty is not included there.

Modeling uncertainties: Uncertainties in the modeling of the signal and background processes may impact the acceptance and selection efficiencies, the shape of the fitted distributions, and the predicted cross sections used for the normalization of the simulated event samples. All modeling uncertainties are considered as correlated among data-taking years.

Uncertainties in the simulated event yields due to missing higher-order diagrams in the matrix-

element calculations are evaluated by varying the values of the factorization and renormalization scales. We vary the scales by a factor of two up and down, separately for each scale as well as simultaneously by the same factor, and evaluate the envelope of the six resulting variations to determine the uncertainty in each bin. The resulting shape uncertainty is evaluated for all backgrounds that are estimated from simulation. For the signal process, the effect from these variations on the predicted cross section is not included as a systematic uncertainty.

For the signal process, the effect of the energy scale in initial- and final-state radiation (ISR and FSR) in the parton shower simulation is taken into account as a shape uncertainty. The effect of the color-reconnection model is evaluated from a comparison of simulated $t\bar{t}W$ events simulated with alternative models [77], and an uncertainty of 1% is assigned to cover the observed differences. The effect on the shape of the signal due to the PDF uncertainty is also taken into account as a shape uncertainty, following the procedure described in Ref. [78]. Using the Hessian NNPDF3.1 set [38], the difference with respect to the central value is computed for each of the 100 PDF variations, and these variations are added in quadrature. Then, the α_s variation is taken into account, adding the variation in quadrature.

8 Results

A binned profile likelihood fit is performed on data using the predicted distributions for the signal and background processes [79, 80] in order to extract the production rate of the $t\bar{t}W$ process. The fit is based on a likelihood function L built from the Poisson probabilities to obtain the observed yields given the predicted signal and background estimates, and includes terms for the systematic uncertainties and their correlations. In the dilepton signal region, the NN output score in eight categories defined by lepton flavor and charge is used. In the trilepton signal region, the $m(3\ell)$ distributions are fitted using twelve event categories defined by the jet and medium b-tagged jet multiplicities, as well as the charges of the leptons, as defined in Section 5. The fit further includes the event yields in the control region enriched in WZ and $t\bar{t}Z$ events (in 48 bins grouped by the number of jets and b-tagged jets, and lepton flavors), and in the control region enriched in WZ and $t\bar{t}Z$ events (in four bins grouped by the number of jets, b-tagged jets, and Z candidates), as defined in Section 6. All of the event categories are further split into the three data-taking years.

Rate uncertainties are represented in the likelihood fit by a log-normal probability density function, and shape uncertainties are assumed to follow a Gaussian function. Statistical fluctuations in the yields are taken into account through a single nuisance parameter for all processes [81, 82].

A comparison between the total number of observed and predicted events obtained before the fit in the dilepton and trilepton channels is shown in Table 1. Good agreement between data and the total signal plus background prediction within the systematic uncertainties is observed for each channel.

The observed and predicted NN discriminant distributions are shown in Fig. 7 for events with positive (left) and negative (right) charged leptons in the dilepton signal region, before (prefit, upper) and after (postfit, lower) the fit to the data. Since the lepton charges are input variables in the NN training, the NN is able to separately optimize the separation of signal and background for events with positive and negative lepton charges. As a result, the shapes of the NN discriminant distributions are different for the two classes of events. Figures 8 and 9 show the $m(3\ell)$ distributions for events in the trilepton signal region with total trilepton charge +1 and -1, respectively. The prefit (postfit) distributions are shown in the upper (lower) panels, with

Table 1: Number of predicted and observed events in the dilepton and trilepton signal regions before the fit to the data. The uncertainties in the predicted number of events include both the statistical and systematic components. The uncertainties in the total number of predicted background and background plus signal events in each channel are also given. The symbol “—” indicates that the corresponding background does not apply.

Process	$\ell^+\ell^+$	$\ell^-\ell^-$	$\ell^\pm\ell^\mp\ell^+$	$\ell^\pm\ell^\mp\ell^-$
$t\bar{t}W$	677 ± 21	355 ± 12	119.4 ± 9.2	65.3 ± 5.4
Nonprompt	2490 ± 600	2360 ± 570	325 ± 75	298 ± 71
Charge misID	520 ± 110	520 ± 111	—	—
$t\bar{t}H$	167 ± 34	169 ± 34	56 ± 12	57 ± 12
$t\bar{t}Z/\gamma^*$	335 ± 26	333 ± 26	145 ± 13	147 ± 13
Diboson	382 ± 88	285 ± 65	46.8 ± 9.1	38.0 ± 7.5
Other	178 ± 34	126 ± 27	43.4 ± 8.2	33.5 ± 7.4
Conversions	177 ± 54	192 ± 59	22.9 ± 7.1	24.0 ± 7.4
Total background	4250 ± 620	4000 ± 590	639 ± 80	600 ± 76
Total prediction	4920 ± 620	4350 ± 590	758 ± 81	663 ± 76
Data	5143	4486	834	744

events having 2 (left) and 3 (right) jets, of which exactly 2 are medium b-tagged jets, in both figures.

The sources and estimates of the various systematic uncertainties relevant to this measurement are given in Table 2. The reduction in the uncertainties between the prefit and postfit values is clearly evident in Figs. 7–9. This is due to the categorization of the signal regions and the inclusion of the various control regions in the fit, both of which help to constrain some of the uncertainty sources. The dominant experimental uncertainties include those in the integrated luminosity measurement, the background estimation of electron charge misidentification, and the b jet identification efficiency. The normalization uncertainties in the predictions of the $t\bar{t}H$, VVV , and $t\bar{t}VV$ processes also represent substantial contributions to the total uncertainty in the measurement. Given the similarities of the decay products of these rare processes with those of the $t\bar{t}W$ signal process, they make a sizable contribution to the total uncertainty despite their low number of expected events. Additional important sources arise from the modeling uncertainties associated with the simulation of $t\bar{t}W$ events and from the statistical uncertainty in the predicted number of signal and background events.

Compared to the previous CMS measurement of $t\bar{t}W$ production [10], which was performed with a subset of the data analyzed here, we achieve a significant improvement in the precision of the cross section measurement, with a reduction of the statistical (systematic) uncertainty by a factor of three (more than two). This is mainly attributed to the larger data sample, as well as to an optimized analysis strategy and improved estimates of the dominant background contributions using data control samples. A higher selection efficiency of $t\bar{t}W$ events and a stronger background suppression of the nonprompt-lepton background contribution is achieved by the lepton selection with the dedicated lepton MVA discriminant. An additional source of improvement in the obtained signal-to-background ratio is associated with the enhanced b tagging performance following the installation of the new pixel detector in 2017 and a more performant b tagging algorithm [57–59].

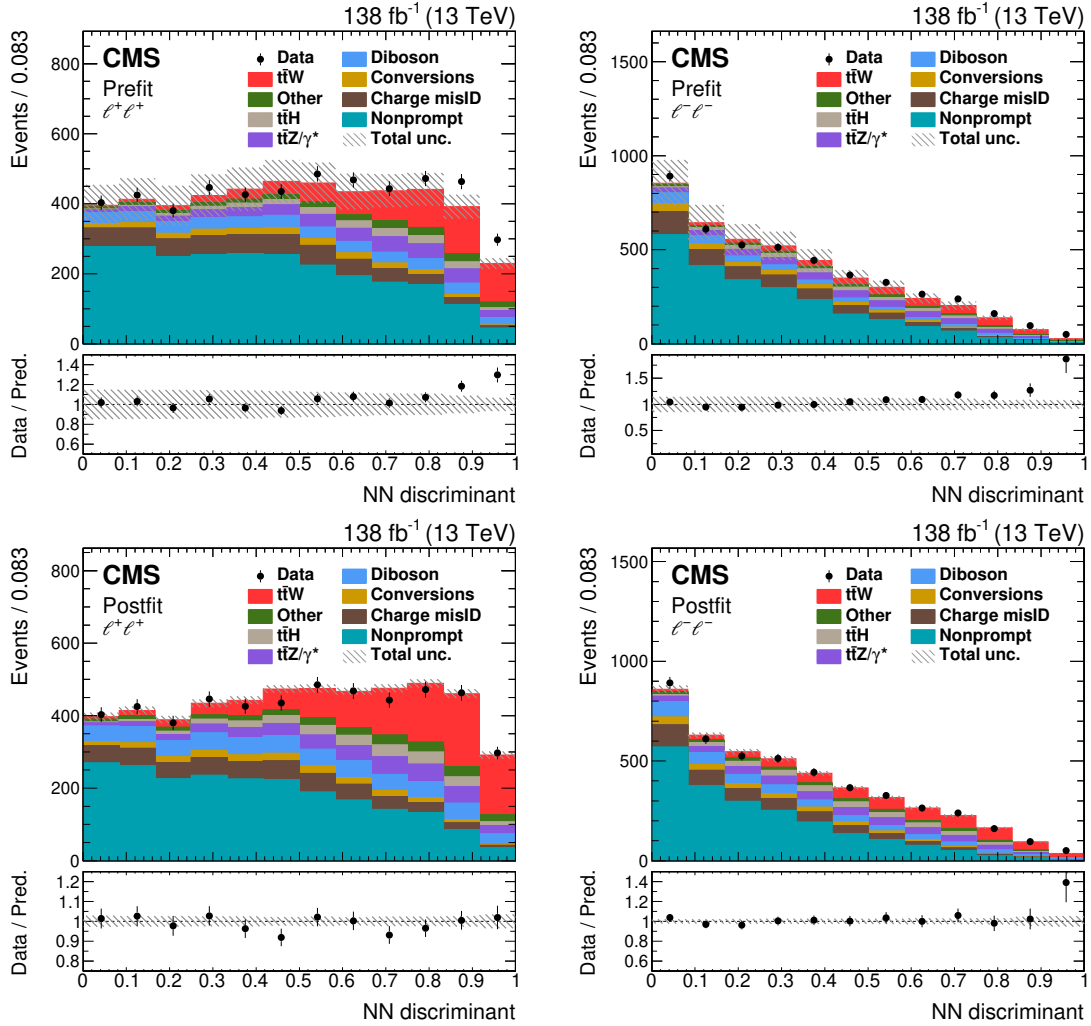


Figure 7: Comparison of the number of observed (points) and predicted (colored histograms) events in the same-sign dilepton signal region. The distributions of the NN output score are displayed in final states with two leptons of positive (left) and negative (right) charges. The predictions are shown “prefit” as in Fig. 2 (upper row), and with the values of the normalizations and nuisance parameters obtained in the fit to the data applied (“postfit”, lower row). The vertical bars on the points represent the statistical uncertainties in the data, and the hatched bands the systematic uncertainty in the predictions. In the lower panels, the ratio of the event yields in data to the overall sum of the predictions is presented.

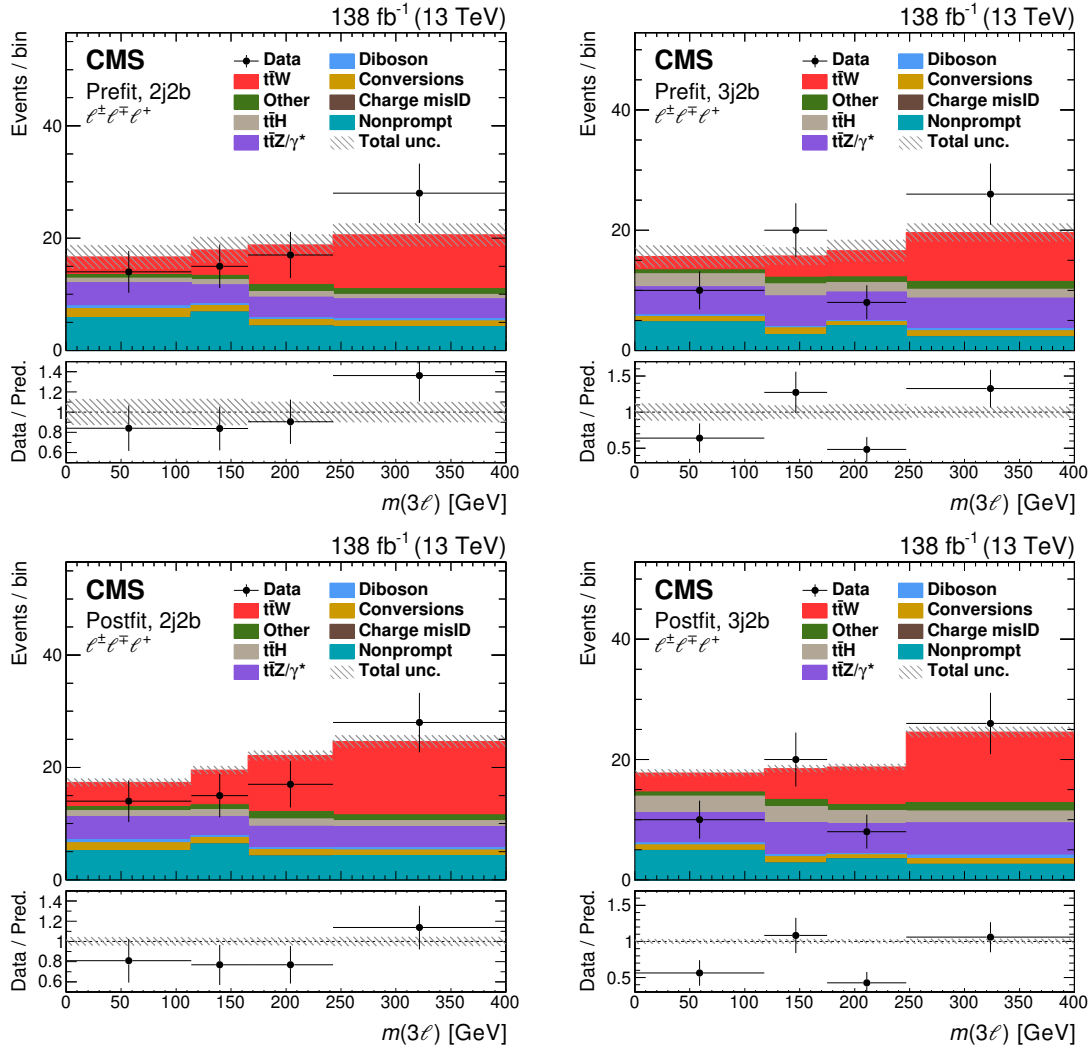


Figure 8: Comparison of the number of observed (points) and predicted (colored histograms) events in the tripleton signal region with positive sum of lepton charges. The distributions of the three-lepton invariant mass are displayed in final states with two (left) and three (right) jets, of which exactly two pass the medium b tagging requirements. The predictions are shown “prefit” as in Fig. 3 (upper row), and with the values of the normalizations and nuisance parameters obtained in the fit to the data applied (“postfit”, lower row). The vertical bars on the points represent the statistical uncertainties in the data, the horizontal bars the bin widths, and the hatched bands the systematic uncertainty in the predictions. The last bins include the overflow contributions. In the lower panels, the ratio of the event yields in data to the overall sum of the predictions is presented.

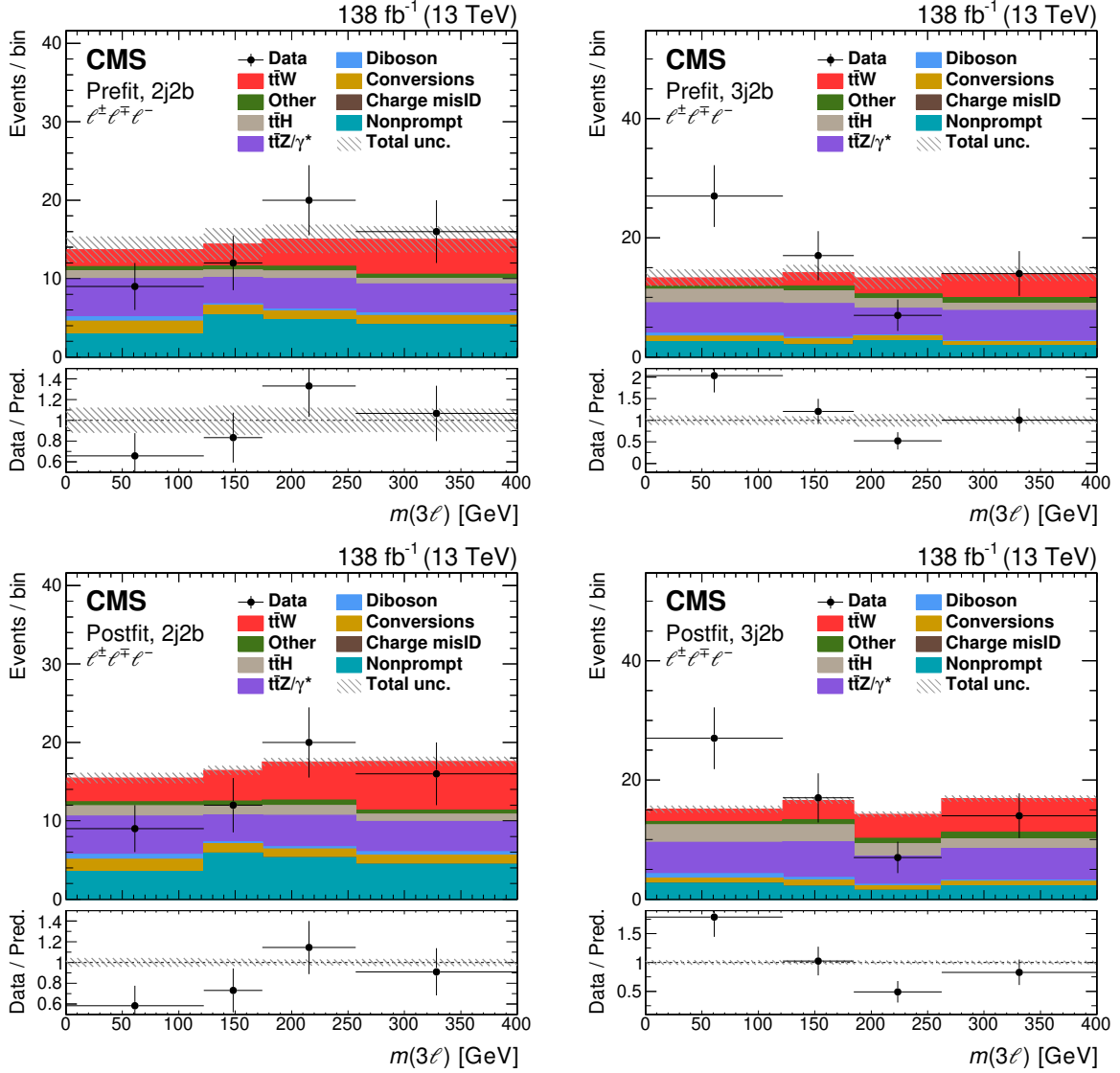


Table 2: Sources of systematic uncertainty in the predicted signal and background event yields with their impact on the measured $t\bar{t}W$ production cross section, estimated after the fit to the data. Only systematic uncertainty sources with values greater than 0.1% are included in the table. The production cross sections of the $t\bar{t}W$, WZ , ZZ , and $t\bar{t}Z$ processes are simultaneously constrained in the fit. The second-to-last row refers to the statistical uncertainty in the simulated event samples.

Source	Uncertainty [%]
Experimental uncertainties	
Integrated luminosity	1.9
b tagging efficiency	1.6
Trigger efficiency	1.2
Pileup reweighting	1.0
L1 inefficiency	0.7
Jet energy scale	0.6
Jet energy resolution	0.4
Lepton selection efficiency	0.4
Background uncertainties	
$t\bar{t}H$ normalization	2.6
Charge misidentification	1.6
Nonprompt leptons	1.3
VVV normalization	1.2
$t\bar{t}VV$ normalization	1.2
Conversions normalization	0.7
$t\bar{t}\gamma$ normalization	0.6
ZZ normalization	0.6
Other normalizations	0.5
$t\bar{t}Z$ normalization	0.3
WZ normalization	0.2
tZq normalization	0.2
tHq normalization	0.2
Modeling uncertainties	
$t\bar{t}W$ scale	1.8
$t\bar{t}W$ color reconnection	1.0
ISR & FSR scale for $t\bar{t}W$	0.8
$t\bar{t}\gamma$ scale	0.4
VVV scale	0.3
$t\bar{t}H$ scale	0.2
Conversions	0.2
Simulation statistical uncertainty	1.8
Total systematic uncertainty	5.8

The measured $t\bar{t}W$ inclusive cross section is shown in Table 3 with its complete statistical and systematic uncertainties. A comparison of the measured $\sigma_{t\bar{t}W}$ values obtained from this analysis using different final states separately is shown in Fig. 10. In addition, two SM predictions are shown both in Table 3 and Fig. 10. The measured cross section is larger than but consistent with both the SM NLO+NNLL calculation [16] and the SM prediction using NLO plus an improved FxFx merging procedure [21]. A large measured $t\bar{t}W$ cross section value when compared to the SM predictions is consistent with the results on $t\bar{t}W$ production from $t\bar{t}H$ and $t\bar{t}\bar{t}$ studies from Refs. [12, 13].

Table 3: Summary of measured and predicted production cross sections of $t\bar{t}W$, $t\bar{t}W^+$, and $t\bar{t}W^-$ production, as well as of the $\sigma_{t\bar{t}W^+}/\sigma_{t\bar{t}W^-}$ ratio. The SM predictions quoted at NLO+NNLL accuracy are taken from Refs. [15, 16]. The SM predictions quoted at NLO accuracy and including corrections from an improved FxFx merging procedure (NLO+FxFx) have been provided by the authors of Ref. [21]. The theoretical uncertainties include scale variations and PDF uncertainties.

Observable	Measurement	SM prediction	
		NLO+NNLL	NLO+FxFx
$\sigma_{t\bar{t}W}$	868 ± 40 (stat) ± 51 (syst) fb	592^{+155}_{-97} (theo) fb	722^{+71}_{-78} (theo) fb
$\sigma_{t\bar{t}W^+}$	553 ± 30 (stat) ± 30 (syst) fb	384^{+53}_{-33} (theo) fb	475^{+46}_{-52} (theo) fb
$\sigma_{t\bar{t}W^-}$	343 ± 26 (stat) ± 25 (syst) fb	198^{+26}_{-17} (theo) fb	247^{+24}_{-27} (theo) fb
$\sigma_{t\bar{t}W^+}/\sigma_{t\bar{t}W^-}$	1.61 ± 0.15 (stat) $^{+0.07}_{-0.05}$ (syst)	$1.94^{+0.37}_{-0.24}$ (theo)	$1.92^{+0.27}_{-0.29}$ (theo)

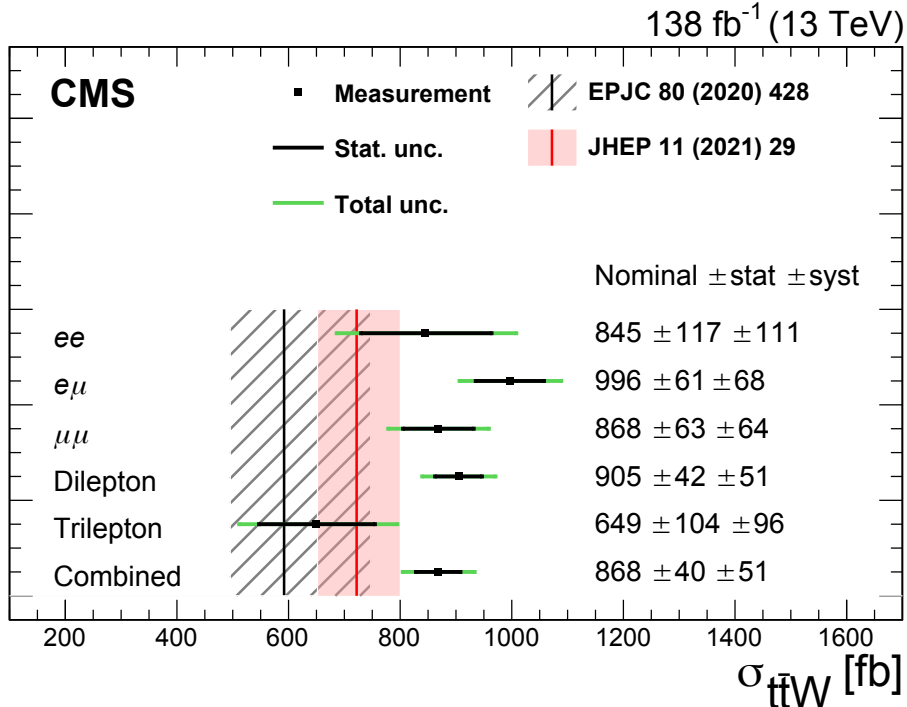


Figure 10: The measured $t\bar{t}W$ production cross section for the individual dilepton (ee , $e\mu$, $\mu\mu$, and combined) channels and the tripleton channel, as well as their combination. The inner black bars show the statistical uncertainty, and the outer green bars give the total uncertainty. The predictions from two SM calculations from Refs. [16, 21] are shown by the black and red vertical lines, with the associated bands corresponding to the total uncertainty.

The separate $t\bar{t}W^+$ and $t\bar{t}W^-$ cross section measurements are of special interest because of the enhancement in pp collisions of the former with respect to the latter due to valence quark effects, and therefore provide important information on the PDF of the proton. The cross sections are measured in a simultaneous fit to data, where the events in categories with positive (negative) sum of lepton charges are used to constrain the $t\bar{t}W^+$ ($t\bar{t}W^-$) cross section. The resulting cross sections and corresponding uncertainties are given in Table 3 and shown in Fig. 11. The correlation between the two measured cross sections originates from the use of common nuisance parameters and the same control regions in the fit. The sum of the two measured cross sections is consistent with the measured inclusive $t\bar{t}W$ cross section within the statistical uncertainties. Both cross sections are larger than but consistent with the SM NLO+NNLL calculations from Ref. [15] and the SM NLO predictions using an improved FxFx merging procedure provided by the authors of Ref. [21]. These predictions and their uncertainties are shown in Table 3.

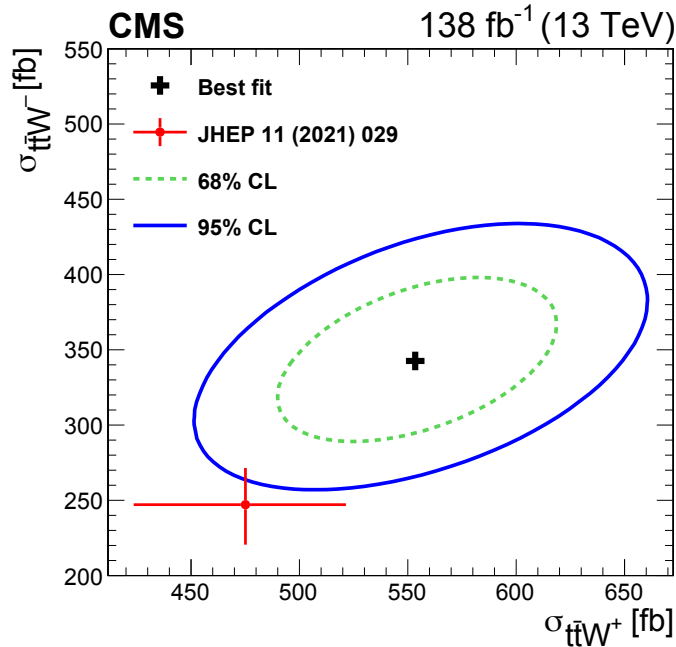


Figure 11: The measurement of the $t\bar{t}W^+$ vs. $t\bar{t}W^-$ cross sections (black cross), along with the 68 (green dashed) and 95% (blue solid) CL intervals. The SM prediction provided by the authors of Ref. [21] is shown by the red dot, with the horizontal and vertical bars corresponding to the total uncertainties.

The measurement of the ratio between the cross sections of the two processes, $\sigma_{t\bar{t}W^+}/\sigma_{t\bar{t}W^-}$, is performed by modifying the fit procedure to directly measure the ratio. Figure 12 shows the scan of the negative log-likelihood, with the accompanying best fit value and 68 and 95% confidence level (CL) intervals for the ratio. The ratio measurement has a reduced relative systematic uncertainty compared to the individual cross sections because of partial correlations between some of the uncertainty sources that cancel in the ratio. The measured ratio is smaller than both the SM NLO+NNLL calculation from Ref. [15] and the SM NLO+FxFx prediction provided by the authors of Ref. [21], all shown in Table 3. The $t\bar{t}W$ production cross section and the ratio $\sigma_{t\bar{t}W^+}/\sigma_{t\bar{t}W^-}$ are measured with total uncertainties that are a factor of two smaller than the uncertainties associated with the corresponding SM predictions [15, 16, 21].

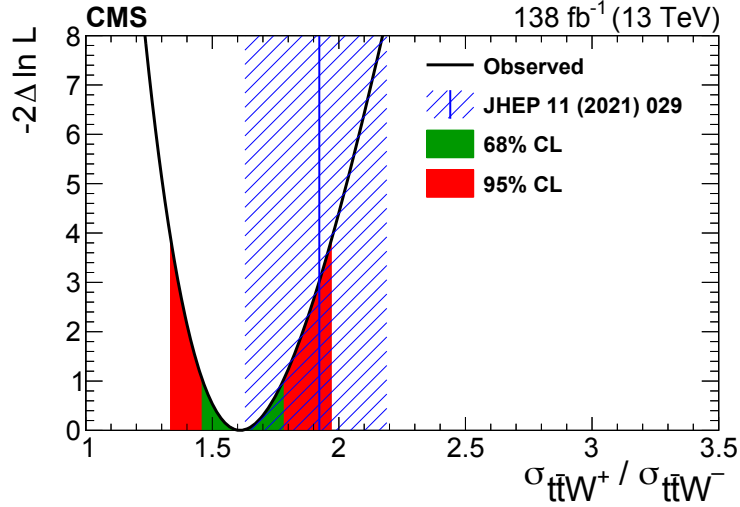


Figure 12: The scan of the negative log-likelihood used in the measurement of the cross section ratio $\sigma_{t\bar{t}W^+}/\sigma_{t\bar{t}W^-}$. The best fit value is indicated, with the inner green and outer red bands displaying the 68 and 95% CL intervals, respectively. An SM prediction and its uncertainty, found from the cross section values provided by the authors of Ref. [21], are shown by the vertical blue line and hatched blue band.

9 Summary

The cross section of the associated production of a W boson with a top quark-antiquark pair ($t\bar{t}W$) in proton-proton collisions at $\sqrt{s} = 13$ TeV is measured using data collected with the CMS detector in 2016–2018, corresponding to an integrated luminosity of 138 fb^{-1} . The measurement is performed in events with two same-sign or three charged leptons (electrons and muons) and additional jets. Events are categorized according to the charges and flavors of the leptons, and the number of jets and jets from the hadronization of b quarks. In the dilepton channel, a multiclass neural network is used to improve the separation of signal from background processes. In the trilepton channel, the invariant mass of the three leptons is used as the discriminating variable. Background contributions with leptons originating from hadron decays, jets or hadrons misidentified as leptons, and with misreconstructed charge are estimated from control samples in data. All other background processes are estimated from simulated event samples, and control samples in data are used to constrain the dominant contributions.

The inclusive $t\bar{t}W$ production cross section in the full phase space is measured to be 868 ± 40 (stat) ± 51 (syst) fb. The $t\bar{t}W^+$ and $t\bar{t}W^-$ cross sections are also determined as 553 ± 30 (stat) ± 30 (syst) and 343 ± 26 (stat) ± 25 (syst) fb, respectively. The measured ratio between these production cross sections is 1.61 ± 0.15 (stat) $^{+0.07}_{-0.05}$ (syst). The measured cross sections are larger than but consistent with standard model predictions, while the $\sigma_{t\bar{t}W^+}/\sigma_{t\bar{t}W^-}$ ratio is smaller than but consistent with the predicted value. These results are all consistent with earlier measurements and are the most precise determinations published to date.

References

- [1] O. Bessidskaia Bylund et al., “Probing top quark neutral couplings in the standard model effective field theory at NLO in QCD”, *JHEP* **05** (2016) 052, doi:10.1007/JHEP05(2016)052, arXiv:1601.08193.

- [2] J. Dror, M. Farina, E. Salvioni, and J. Serra, “Strong tW scattering at the LHC”, *JHEP* **01** (2016) 071, doi:10.1007/JHEP01(2016)071, arXiv:1511.03674.
- [3] A. Buckley et al., “Constraining top quark effective theory in the LHC Run II era”, *JHEP* **04** (2016) 015, doi:10.1007/JHEP04(2016)015, arXiv:1512.03360.
- [4] F. Maltoni, M. Mangano, I. Tsinikos, and M. Zaro, “Top-quark charge asymmetry and polarization in $t\bar{t}W^\pm$ production at the LHC”, *Phys. Lett. B* **736** (2014) 252, doi:10.1016/j.physletb.2014.07.033, arXiv:1406.3262.
- [5] R. Frederix, D. Pagani, and M. Zaro, “Large NLO corrections in $t\bar{t}W^\pm$ and $t\bar{t}\bar{t}$ hadroproduction from supposedly subleading EW contributions”, *JHEP* **02** (2018) 031, doi:10.1007/JHEP02(2018)031, arXiv:1711.02116.
- [6] CMS Collaboration, “Measurement of associated production of vector bosons and $t\bar{t}$ at $\sqrt{s} = 7$ TeV”, *Phys. Rev. Lett.* **110** (2013) 172002, doi:10.1103/PhysRevLett.110.172002, arXiv:1303.3239.
- [7] ATLAS Collaboration, “Measurement of the $t\bar{t}W$ and $t\bar{t}Z$ production cross sections in pp collisions at $\sqrt{s} = 8$ TeV with the ATLAS detector”, *JHEP* **11** (2015) 172, doi:10.1007/JHEP11(2015)172, arXiv:1509.05276.
- [8] CMS Collaboration, “Observation of top quark pairs produced in association with a vector boson in pp collisions at $\sqrt{s} = 8$ TeV”, *JHEP* **01** (2016) 096, doi:10.1007/JHEP01(2016)096, arXiv:1510.01131.
- [9] ATLAS Collaboration, “Measurement of the $t\bar{t}Z$ and $t\bar{t}W$ production cross sections in multilepton final states using 3.2 fb^{-1} of pp collisions at $\sqrt{s} = 13$ TeV with the ATLAS detector”, *Eur. Phys. J. C* **77** (2017) 40, doi:10.1140/epjc/s10052-016-4574-y, arXiv:1609.01599.
- [10] CMS Collaboration, “Measurement of the cross section for top quark pair production in association with a W or Z boson in proton-proton collisions at $\sqrt{s} = 13$ TeV”, *JHEP* **08** (2018) 011, doi:10.1007/JHEP08(2018)011, arXiv:1711.02547.
- [11] ATLAS Collaboration, “Measurement of the $t\bar{t}Z$ and $t\bar{t}W$ cross sections in proton-proton collisions at $\sqrt{s} = 13$ TeV with the ATLAS detector”, *Phys. Rev. D* **99** (2019) 072009, doi:10.1103/PhysRevD.99.072009, arXiv:1901.03584.
- [12] CMS Collaboration, “Measurement of the Higgs boson production rate in association with top quarks in final states with electrons, muons, and hadronically decaying tau leptons at $\sqrt{s} = 13$ TeV”, *Eur. Phys. J. C* **81** (2021) 378, doi:10.1140/epjc/s10052-021-09014-x, arXiv:2011.03652.
- [13] CMS Collaboration, “Search for production of four top quarks in final states with same-sign or multiple leptons in proton-proton collisions at $\sqrt{s} = 13$ TeV”, *Eur. Phys. J. C* **80** (2020) 75, doi:10.1140/epjc/s10052-019-7593-7, arXiv:1908.06463.
- [14] ATLAS Collaboration, “Evidence for $t\bar{t}\bar{t}$ production in the multilepton final state in proton-proton collisions at $\sqrt{s} = 13$ TeV with the ATLAS detector”, *Eur. Phys. J. C* **80** (2020) 1085, doi:10.1140/epjc/s10052-020-08509-3, arXiv:2007.14858.
- [15] A. Broggio et al., “Top-quark pair hadroproduction in association with a heavy boson at NLO+NNLL including EW corrections”, *JHEP* **08** (2019) 039, doi:10.1007/JHEP08(2019)039, arXiv:1907.04343.

-
- [16] A. Kulesza et al., “Associated top quark pair production with a heavy boson: differential cross sections at NLO+NNLL accuracy”, *Eur. Phys. J. C* **80** (2020) 428, doi:10.1140/epjc/s10052-020-7987-6, arXiv:2001.03031.
- [17] G. Bevilacqua et al., “NLO QCD corrections to off-shell $t\bar{t}W^\pm$ production at the LHC: correlations and asymmetries”, *Eur. Phys. J. C* **81** (2021) 675, doi:10.1140/epjc/s10052-021-09478-x, arXiv:2012.01363.
- [18] S. von Buddenbrock, R. Ruiz, and B. Mellado, “Anatomy of inclusive $t\bar{t}W$ production at hadron colliders”, *Phys. Lett. B* **811** (2020) 135964, doi:10.1016/j.physletb.2020.135964, arXiv:2009.00032.
- [19] R. Frederix and I. Tsinikos, “Subleading EW corrections and spin-correlation effects in $t\bar{t}W$ multi-lepton signatures”, *Eur. Phys. J. C* **80** (2020) 803, doi:10.1140/epjc/s10052-020-8388-6, arXiv:2004.09552.
- [20] F. Febres Cordero, M. Kraus, and L. Reina, “Top-quark pair production in association with a W^\pm gauge boson in the POWHEG-BOX”, *Phys. Rev. D* **103** (2021) 094014, doi:10.1103/PhysRevD.103.094014, arXiv:2101.11808.
- [21] R. Frederix and I. Tsinikos, “On improving NLO merging for $t\bar{t}W$ production”, *JHEP* **11** (2021) 29, doi:10.1007/JHEP11(2021)029, arXiv:2108.07826.
- [22] G. Bevilacqua et al., “Modeling uncertainties of $t\bar{t}W^\pm$ multilepton signatures”, *Phys. Rev. D* **105** (2022) 014018, doi:10.1103/PhysRevD.105.014018, arXiv:2109.15181.
- [23] HEPData record for this analysis, 2022. doi:10.17182/hepdata.127991.
- [24] CMS Collaboration, “The CMS experiment at the CERN LHC”, *JINST* **3** (2008) S08004, doi:10.1088/1748-0221/3/08/S08004.
- [25] CMS Collaboration, “Performance of the CMS Level-1 trigger in proton-proton collisions at $\sqrt{s} = 13$ TeV”, *JINST* **15** (2020) P10017, doi:10.1088/1748-0221/15/10/P10017, arXiv:2006.10165.
- [26] CMS Collaboration, “The CMS trigger system”, *JINST* **12** (2017) P01020, doi:10.1088/1748-0221/12/01/P01020, arXiv:1609.02366.
- [27] G. Bevilacqua et al., “The simplest of them all: $t\bar{t}W^\pm$ at NLO accuracy in QCD”, *JHEP* **08** (2020) 043, doi:10.1007/JHEP08(2020)043, arXiv:2005.09427.
- [28] J. Alwall et al., “The automated computation of tree-level and next-to-leading order differential cross sections, and their matching to parton shower simulations”, *JHEP* **07** (2014) 079, doi:10.1007/JHEP07(2014)079, arXiv:1405.0301.
- [29] P. Nason, “A new method for combining NLO QCD with shower Monte Carlo algorithms”, *JHEP* **11** (2004) 040, doi:10.1088/1126-6708/2004/11/040, arXiv:hep-ph/0409146.
- [30] S. Frixione, P. Nason, and C. Oleari, “Matching NLO QCD computations with parton shower simulations: the POWHEG method”, *JHEP* **11** (2007) 070, doi:10.1088/1126-6708/2007/11/070, arXiv:0709.2092.
- [31] S. Alioli, P. Nason, C. Oleari, and E. Re, “A general framework for implementing NLO calculations in shower Monte Carlo programs: the POWHEG BOX”, *JHEP* **06** (2010) 043, doi:10.1007/JHEP06(2010)043, arXiv:1002.2581.

- [32] T. Sjöstrand et al., “An introduction to PYTHIA 8.2”, *Comput. Phys. Commun.* **191** (2015) 159, doi:10.1016/j.cpc.2015.01.024, arXiv:1410.3012.
- [33] J. Alwall et al., “Comparative study of various algorithms for the merging of parton showers and matrix elements in hadronic collisions”, *Eur. Phys. J. C* **53** (2008) 473, doi:10.1140/epjc/s10052-007-0490-5, arXiv:0706.2569.
- [34] R. Frederix and S. Frixione, “Merging meets matching in MC@NLO”, *JHEP* **12** (2012) 061, doi:10.1007/JHEP12(2012)061, arXiv:1209.6215.
- [35] S. Agostinelli et al., “GEANT4—a simulation toolkit”, *Nucl. Instrum. Meth. A* **506** (2003) 250, doi:10.1016/S0168-9002(03)01368-8.
- [36] CMS Collaboration, “Measurement of the inclusive production cross sections for forward jets and for dijet events with one forward and one central jet in pp collisions at $\sqrt{s} = 7$ TeV”, *JHEP* **06** (2012) 036, doi:10.1007/JHEP06(2012)036, arXiv:1202.0704.
- [37] CMS Collaboration, “Measurement of the inelastic proton-proton cross section at $\sqrt{s} = 7$ TeV”, *Phys. Lett. B* **722** (2013) 5, doi:10.1016/j.physletb.2013.03.024, arXiv:1210.6718.
- [38] NNPDF Collaboration, “Parton distributions from high-precision collider data”, *Eur. Phys. J. C* **77** (2017) 663, doi:10.1140/epjc/s10052-017-5199-5, arXiv:1706.00428.
- [39] P. Skands, S. Carrazza, and J. Rojo, “Tuning PYTHIA 8.1: the Monash 2013 tune”, *Eur. Phys. J. C* **74** (2014) 3024, doi:10.1140/epjc/s10052-014-3024-y, arXiv:1404.5630.
- [40] CMS Collaboration, “Extraction and validation of a new set of CMS PYTHIA 8 tunes from underlying-event measurements”, *Eur. Phys. J. C* **80** (2020) 4, doi:10.1140/epjc/s10052-019-7499-4, arXiv:1903.12179.
- [41] NNPDF Collaboration, “Parton distributions for the LHC run II”, *JHEP* **04** (2015) 040, doi:10.1007/JHEP04(2015)040, arXiv:1410.8849.
- [42] CMS Collaboration, “Event generator tunes obtained from underlying event and multiparton scattering measurements”, *Eur. Phys. J. C* **76** (2016) 155, doi:10.1140/epjc/s10052-016-3988-x, arXiv:1512.00815.
- [43] CMS Collaboration, “Investigations of the impact of the parton shower tuning in PYTHIA 8 in the modelling of $t\bar{t}$ at $\sqrt{s} = 8$ and 13 TeV”, CMS Physics Analysis Summary CMS-PAS-TOP-16-021, 2016.
- [44] CMS Collaboration, “Particle-flow reconstruction and global event description with the CMS detector”, *JINST* **12** (2017) P10003, doi:10.1088/1748-0221/12/10/P10003, arXiv:1706.04965.
- [45] CMS Collaboration, “Technical proposal for the Phase-II upgrade of the Compact Muon Solenoid”, CMS Technical Proposal CERN-LHCC-2015-010, CMS-TDR-15-02, 2015.
- [46] CMS Collaboration, “Electron and photon reconstruction and identification with the CMS experiment at the CERN LHC”, *JINST* **16** (2021) P05014, doi:10.1088/1748-0221/16/05/P05014, arXiv:2012.06888.

-
- [47] CMS Collaboration, “Performance of the CMS muon detector and muon reconstruction with proton-proton collisions at $\sqrt{s} = 13$ TeV”, *JINST* **13** (2018) P06015, doi:10.1088/1748-0221/13/06/P06015, arXiv:1804.04528.
- [48] CMS Collaboration, “Inclusive and differential cross section measurements of single top quark production in association with a Z boson in proton-proton collisions at $\sqrt{s} = 13$ TeV”, *JHEP* **02** (2022) 107, doi:10.1007/JHEP02(2022)107, arXiv:2111.02860.
- [49] CMS Collaboration, “Measurement of the inclusive and differential $t\bar{t}\gamma$ cross sections in the dilepton channel and effective field theory interpretation in proton-proton collisions at $\sqrt{s} = 13$ TeV”, *JHEP* **05** (2022) 091, doi:10.1007/JHEP05(2022)091, arXiv:2201.07301.
- [50] CMS Collaboration, “Search for new physics in same-sign dilepton events in proton-proton collisions at $\sqrt{s} = 13$ TeV”, *Eur. Phys. J. C* **76** (2016) 439, doi:10.1140/epjc/s10052-016-4261-z, arXiv:1605.03171.
- [51] CMS Collaboration, “Observation of single top quark production in association with a Z boson in proton-proton collisions at $\sqrt{s} = 13$ TeV”, *Phys. Rev. Lett.* **122** (2019) 132003, doi:10.1103/PhysRevLett.122.132003, arXiv:1812.05900.
- [52] CMS Collaboration, “Performance of electron reconstruction and selection with the CMS detector in proton-proton collisions at $\sqrt{s} = 8$ TeV”, *JINST* **10** (2015) P06005, doi:10.1088/1748-0221/10/06/P06005, arXiv:1502.02701.
- [53] M. Cacciari, G. P. Salam, and G. Soyez, “The anti- k_T jet clustering algorithm”, *JHEP* **04** (2008) 063, doi:10.1088/1126-6708/2008/04/063, arXiv:0802.1189.
- [54] M. Cacciari, G. P. Salam, and G. Soyez, “FASTJET user manual”, *Eur. Phys. J. C* **72** (2012) 1896, doi:10.1140/epjc/s10052-012-1896-2, arXiv:1111.6097.
- [55] CMS Collaboration, “Pileup mitigation at CMS in 13 TeV data”, *JINST* **15** (2020) P09018, doi:10.1088/1748-0221/15/09/P09018, arXiv:2003.00503.
- [56] CMS Collaboration, “Jet energy scale and resolution in the CMS experiment in pp collisions at 8 TeV”, *JINST* **12** (2017) P02014, doi:10.1088/1748-0221/12/02/P02014, arXiv:1607.03663.
- [57] CMS Collaboration, “Identification of heavy-flavour jets with the CMS detector in pp collisions at 13 TeV”, *JINST* **13** (2018) P05011, doi:10.1088/1748-0221/13/05/P05011, arXiv:1712.07158.
- [58] E. Bols et al., “Jet flavour classification using DeepJet”, *JINST* **15** (2020) P12012, doi:10.1088/1748-0221/15/12/P12012, arXiv:2008.10519.
- [59] CMS Collaboration, “Performance of the DeepJet b tagging algorithm using 41.9 fb^{-1} of data from proton-proton collisions at 13 TeV with Phase 1 CMS detector”, CMS Detector Performance Note CMS-DP-2018-058, 2018.
- [60] CMS Collaboration, “Performance of missing transverse momentum reconstruction in proton-proton collisions at $\sqrt{s} = 13$ TeV using the CMS detector”, *JINST* **14** (2019) P07004, doi:10.1088/1748-0221/14/07/P07004, arXiv:1903.06078.

- [61] Particle Data Group, P. A. Zyla et al., “Review of particle physics”, *Prog. Theor. Exp. Phys.* **2020** (2020) 083C01, doi:10.1093/ptep/ptaa104.
- [62] X. Glorot, A. Bordes, and Y. Bengio, “Deep sparse rectifier neural networks”, in *Proc. 14th Int. Conf. on Artificial Intelligence and Statistics (AISTATS 2011): Fort Lauderdale, FL, USA, April 11–13, 2011*. 2011. *Proc. Mach. Learn. Res.* **15** (2011) 315.
- [63] M. Abadi et al., “TENSORFLOW: large-scale machine learning on heterogeneous distributed systems”, 2016. arXiv:1603.04467.
- [64] F. Chollet et al., “KERAS”, 2015. <https://github.com/fchollet/keras>.
- [65] D. P. Kingma and J. Ba, “ADAM: a method for stochastic optimization”, in *Proc. 3rd Int. Conf. on Learning Representations (ICLR 2015): San Diego, CA, USA, May 7–9, 2015*. 2015. arXiv:1412.6980.
- [66] I. Goodfellow, Y. Bengio, and A. Courville, “Deep learning”. MIT Press, Cambridge, MA, USA, 2016. <http://www.deeplearningbook.org>.
- [67] N. Srivastava et al., “Dropout: a simple way to prevent neural networks from overfitting”, *J. Mach. Learn. Res.* **15** (2014) 1929.
- [68] CMS Collaboration, “Evidence for associated production of a Higgs boson with a top quark pair in final states with electrons, muons, and hadronically decaying τ leptons at $\sqrt{s} = 13$ TeV”, *JHEP* **08** (2018) 066, doi:10.1007/JHEP08(2018)066, arXiv:1803.05485.
- [69] CMS Collaboration, “Precision luminosity measurement in proton-proton collisions at $\sqrt{s} = 13$ TeV in 2015 and 2016 at CMS”, *Eur. Phys. J. C* **81** (2021) 800, doi:10.1140/epjc/s10052-021-09538-2, arXiv:2104.01927.
- [70] CMS Collaboration, “CMS luminosity measurement for the 2017 data-taking period at $\sqrt{s} = 13$ TeV”, CMS Physics Analysis Summary CMS-PAS-LUM-17-004, 2018.
- [71] CMS Collaboration, “CMS luminosity measurement for the 2018 data-taking period at $\sqrt{s} = 13$ TeV”, CMS Physics Analysis Summary CMS-PAS-LUM-18-002, 2019.
- [72] CMS Collaboration, “Measurement of the inclusive and differential $t\bar{t}\gamma$ cross sections in the single-lepton channel and EFT interpretation at $\sqrt{s} = 13$ TeV”, *JHEP* **12** (2021) 180, doi:10.1007/JHEP12(2021)180, arXiv:2107.01508.
- [73] CMS Collaboration, “Search for electroweak production of charginos and neutralinos in multilepton final states in proton-proton collisions at $\sqrt{s} = 13$ TeV”, *JHEP* **03** (2018) 166, doi:10.1007/JHEP03(2018)166, arXiv:1709.05406.
- [74] CMS Collaboration, “A portrait of the Higgs boson by the CMS experiment ten years after the discovery”, *Nature* **607** (2022) 60, doi:10.1038/s41586-022-04892-x, arXiv:2207.00043.
- [75] CMS Collaboration, “Search for standard model production of four top quarks with same-sign and multilepton final states in proton-proton collisions at $\sqrt{s} = 13$ TeV”, *Eur. Phys. J. C* **78** (2018) 140, doi:10.1140/epjc/s10052-018-5607-5, arXiv:1710.10614.

- [76] CMS Collaboration, "Observation of the production of three massive gauge bosons at $\sqrt{s} = 13$ TeV", *Phys. Rev. Lett.* **125** (2020) 151802, doi:10.1103/PhysRevLett.125.151802, arXiv:2006.11191.
- [77] CMS Collaboration, "CMS PYTHIA 8 colour reconnection tunes based on underlying-event data", 2022. arXiv:2205.02905. Submitted to *Eur. Phys. J. C*.
- [78] J. Butterworth et al., "PDF4LHC recommendations for LHC Run II", *J. Phys. G* **43** (2016) 023001, doi:10.1088/0954-3899/43/2/023001, arXiv:1510.03865.
- [79] ATLAS and CMS Collaborations, and LHC Higgs Combination Group, "Procedure for the LHC Higgs boson search combination in Summer 2011", Technical Report CMS-NOTE-2011-005, ATL-PHYS-PUB-2011-11, 2011.
- [80] G. Cowan, K. Cranmer, E. Gross, and O. Vitells, "Asymptotic formulae for likelihood-based tests of new physics", *Eur. Phys. J. C* **71** (2011) 1554, doi:10.1140/epjc/s10052-011-1554-0, arXiv:1007.1727. [Erratum: doi:10.1140/epjc/s10052-013-2501-z].
- [81] R. Barlow and C. Beeston, "Fitting using finite Monte Carlo samples", *Comput. Phys. Commun.* **77** (1993) 219, doi:10.1016/0010-4655(93)90005-w.
- [82] J. S. Conway, "Incorporating nuisance parameters in likelihoods for multisource spectra", in *Proc. 2011 Workshop on Statistical Issues Related to Discovery Claims in Search Experiments and Unfolding (PHYSTAT 2011): Geneva, Switzerland, January 17–20, 2011*. 2011. arXiv:1103.0354. doi:10.5170/CERN-2011-006.115.